Microscopic characterization of the superconducting gap function in $Sn_{1-x}In_xTe$

T. Nomoto [1,*] M. Kawamura [2] T. Koretsune [3] R. Arita [1,4] T. Machida [4] T. Hanaguri [4] M. Kriener [4] Y. Taguchi [4] and Y. Tokura [4,1,5]

[1]*Department of Applied Physics, The University of Tokyo, Hongo, Bunkyo-ku, Tokyo 113-8656, Japan*
[2]*The Institute for Solid State Physics, The University of Tokyo, Kashiwa-shi, Chiba 277-8581, Japan*
[3]*Department of Physics, Tohoku University, Miyagi 980-8578, Japan*
[4]*RIKEN Center for Emergent Matter Science (CEMS), Wako 351-0198, Japan*
[5]*Tokyo College, The University of Tokyo, Hongo, Bunkyo-ku, Tokyo 113-8656, Japan*

(Received 12 July 2019; revised manuscript received 23 October 2019; published 8 January 2020)

Superconductivity in the doped topological crystalline insulator $Sn_{1-x}In_xTe$ is studied by first-principles calculation based on superconducting density functional theory (SCDFT) and tunneling spectroscopy. By considering the spin-orbit coupling and frequency dependence of the screened Coulomb interaction in SCDFT, we succeed in reproducing the critical temperature of $Sn_{1-x}In_xTe$ quantitatively, in which the spin-orbit coupling is found to play an essential role. The leading gap function is a conventional s wave with moderate anisotropy in $\boldsymbol{k}$ space, and we find that the subdominant odd-parity instability is significantly weaker than the s-wave instability. We perform tunneling spectroscopy measurement and confirm that the spectrum is consistent with the calculated gap function.

DOI: 10.1103/PhysRevB.101.014505

I. INTRODUCTION

Searching for new topological materials is one of the most trending topics in modern condensed matter physics. Especially, topologically nontrivial superconductors [1–5] have been extensively studied owing to their potential applicability to topological quantum computation, in which the manipulation of the Majorana bound states is required [6–9]. Today, two routes of realizing topological superconductors are mainly explored; one is the intrinsic bulk realization and the other is the engineered one in an artificial structure. In the latter case, a combined effect of conventional s-wave gap and topologically nontrivial electronic structure is a key to obtain topological superconductivity [10–14], and recent experiments have detected its signature in several systems including one-dimensional nanowire/chain systems [15–18] and two-dimensional interface/surface systems based on Bi_2Se_3 [19–23] and $FeSe_{0.45}Te_{0.55}$ [24–26]. However, in contrast to the artificial systems, there are a few candidates for the bulk topological superconductors [27,28]. Thus, to detect the Majorana bound states in bulk systems is still a challenging problem.

Recently, it has been reported that a doped topological insulator or topological crystalline insulator exhibits topological superconductivity not only in its interface/surface but also in the bulk. For example, $Cu_xBi_2Se_3$ shows bulk superconductivity with $T_c \sim 3.8$ K at $x = 0.12$ [29–33], and the pronounced zero-bias conductance peak, a signature of the Majorana bound states [34–37], appears in the point contact spectroscopy [38,39]. Recent measurements of the NMR Knight shift show spontaneous spin-rotational symmetry breaking through the superconducting transition [40], which indicates the emergence of spin-triplet superconductivity with the strong spin-orbit coupling. Specific heat measurements under magnetic fields also support the emergence of the nematicity in the superconducting phase [41]. These behaviors are well described by the odd-parity gap function introduced by Fu and Berg, which is time-reversal invariant and topologically nontrivial [41–45]. Another candidate of the bulk topological superconductor is the doped topological crystalline insulator $Sn_{1-x}In_xTe$. The superconductivity develops in topologically nontrivial electronic structure [46,47] by indium doping [48–53], and the zero-bias conductance peak is observed [54]. These superconductors do not break the time-reversal symmetry, and thus, are a new type of topological superconductor belonging to three-dimensional class DIII [55,56].

Above mentioned observations appear to imply existence of a universal mechanism for topological superconductivity arising from the underlying topologically nontrivial insulating states. Although some aspects have been investigated through theoretical calculations, it is yet to be fully understood whether those doped insulators really harbor topological superconductivity. For example, the effective theory discussed by Fu and Berg [42] with a Fermi surface criterion for topological superconductivity [42,57,58] successfully explains observations in $Cu_xBi_2Se_3$, but their assumption for orbital dependent interactions is not yet supported by first-principles calculations. Wan and Savrasov [59] argued that p_z-type gap function is the most stable in $Cu_xBi_2Se_3$, based on the analysis on the momentum dependence of the electron-phonon coupling. However, it does not describe the nematicity observed in experiments [40,41]. In the case of $Sn_{1-x}In_xTe$, there is a proposal that the soft transverse phonon mediates an interorbital attractive interaction, which results in a odd-parity

*nomoto@ap.t.u-tokyo.ac.jp

 ©2020 American Physical Society

pairing state [54,60]. As is shown in Ref. [61], however, the critical temperature of spin-triplet superconductivity never exceeds that of a spin singlet for purely phonon-mediated interactions. That means that quantitative estimation of the screened Coulomb interaction is necessary in considering the competition between the spin-singlet and spin-triplet superconductivity, which has not been done in Ref. [59]. From an experimental point of view, the Majorana bound state is generally elusive in point contact measurements, since it is not the only origin of the zero-bias anomaly [62,63]. The measurement of the NMR Knight shift for $Sn_{1-x}In_xTe$ at $x = 0.04$ indeed detects spin-singlet pair formation [64] and μSR measurements for $x = 0.38$–0.45 support a fully gapped s-wave scenario [65]. It is certain that the sample quality and carrier concentration affect the superconductivity in these compounds [32,66], and thus, calculations and experiments with high accuracy are strongly desired.

In this paper we combined state-of-the-art first-principles calculations and tunneling spectroscopy measurements to investigate the superconducting gap functions and mechanisms in $Sn_{1-x}In_xTe$. We extended density functional theory for superconductivity (SCDFT) to deal with the spin-orbit coupling and odd-parity pairing in an *ab initio* way. Since the electron-phonon coupling and screened Coulomb interaction are calculated without any empirical parameter in SCDFT, it is a suitable method for considering the competition between the spin-singlet and spin-triplet superconductivity. Our SCDFT successfully reproduces the critical temperature T_c for $Sn_{1-x}In_xTe$ quantitatively and reveals that the spin-orbit coupling largely enhances T_c at a low carrier region. The leading gap function is a conventional s wave, and the subdominant odd-parity instability is significantly weaker. We perform a tunneling spectroscopy measurement and confirm that the spectrum is consistent with the calculation, which supports the s-wave scenario. The consistent observations between the theory and experiment in $Sn_{1-x}In_xTe$ are in sharp contrast to those in $Cu_xBi_2Se_3$ (see the Appendix).

II. METHODS

A. Theory

In this section we present a general scheme of SCDFT in which the spin-orbit coupling and odd-parity pairing are considered [67,68]. We assume the time and the space-inversion symmetry, and then the eigenstates for every $\boldsymbol{k}$ point, have twofold Kramer's degeneracy in normal states. Superconductivity in such systems is classified into spin-singlet even-parity or spin-triplet odd-parity state, and here we assume a unitary type gap function, which satisfies $\boldsymbol{d}_n(\boldsymbol{k}) \times \boldsymbol{d}_n^*(\boldsymbol{k}) = \boldsymbol{0}$ where $\boldsymbol{d}_n(\boldsymbol{k})$ is the $\boldsymbol{d}$ vector defined for the band n and the crystal momentum $\boldsymbol{k}$, in the odd-parity state [69]. Within these assumptions, the twofold degeneracy holds in the superconducting states, and thus we can apply the decoupling approximation similar to the even-parity case [67]. Finally, the gap equation becomes almost the same form as the original except for the additional degree of freedom representing the direction of $\boldsymbol{d}$ vector.

The superconducting order parameter $\chi_a(\boldsymbol{r}, \boldsymbol{r}')$ specified by the suffix a ($a = 0$ represents spin-singlet pairing and $a = x, y, z$ each direction of the $\boldsymbol{d}$ vector in spin-triplet pairing) is given by

$$\chi_a(\boldsymbol{r}, \boldsymbol{r}') = \sum_{ib} \frac{\Delta_i^b}{2\varepsilon_i} \tanh\left(\frac{\beta\varepsilon_i}{2}\right) \mathrm{Tr}[\vec{\varphi}_i(\boldsymbol{r})\bar{\sigma}_b\vec{\varphi}_{\bar{i}}^*(\boldsymbol{r}')\bar{\sigma}_a^\dagger], \quad (1)$$

where $\vec{\varphi}_i(\boldsymbol{r})$ is the spinor representation of the normal-state Kohn-Sham orbital with $i = (n, \boldsymbol{k})$ [$\bar{i} = (n, -\boldsymbol{k})$]. β is the inverse temperature and $\bar{\sigma}_a$ is defined as $\bar{\sigma}_a = i\sigma_a\sigma_y$ by using the Pauli matrices σ_a (σ_0 is the 2×2 unit matrix). Energy dispersion of the Bogoliubov quasiparticle ε_i is written by $\varepsilon_i = (\xi_i + \mathrm{Tr}[\Delta_i\Delta_i^\dagger]/2)^{1/2}$ where ξ_i represents the normal-state Kohn-Sham energy and Δ_i is the 2×2 matrix of the gap function whose a component Δ_i^a is defined by $\Delta_i = \sum_a \Delta_i^a\bar{\sigma}^a$. Here Δ_i^a is the most important quantity that should be self-consistently determined by the following gap equation:

$$\Delta_i^a = -\frac{1}{2}\sum_{bj} K_{ab,ij} \tanh\left(\frac{\beta\varepsilon_j}{2}\right)\frac{\Delta_j^b}{\varepsilon_j}, \quad (2)$$

where the interaction kernel $K_{ab,ij}$ is composed of two contributions coming from the electron-phonon coupling and the screened Coulomb interaction,

$$K_{ab,ij} = \frac{K_{ab,ij}^{(\mathrm{ep})} + K_{ab,ij}^{(\mathrm{ee})}}{1 + Z_{ij}}. \quad (3)$$

Here the renormalization factor Z_{ij} does not depend on a and thus is obtained as a simple extension of the previous studies to the spinor representation [67,68]. The two contributions in the kernel are respectively given by

$$K_{ab,ij}^{(\mathrm{ep})} = \sum_{\nu\boldsymbol{q}} \frac{\mathrm{Tr}[\sigma_b^T g_{\nu\boldsymbol{q},ji}\sigma_a^T g_{\nu\boldsymbol{q},ji}^\dagger]}{\tanh(\beta\varepsilon_i/2)\tanh(\beta\varepsilon_j/2)} \times [I(\varepsilon_i, \varepsilon_j, \Omega_{\nu\boldsymbol{q}}) - I(\varepsilon_i, -\varepsilon_j, \Omega_{\nu\boldsymbol{q}})], \quad (4)$$

$$K_{ab,ij}^{(\mathrm{ee})} = \frac{1}{\pi}\int_0^\infty d\omega \frac{|\xi_i| + |\xi_j|}{(|\xi_i| + |\xi_j|)^2 + \omega^2} V_{ab,ij}(\omega), \quad (5)$$

where $\Omega_{\nu\boldsymbol{q}}$ is the phonon frequency of the branch ν with momentum $\boldsymbol{q}$. $I(\varepsilon, \varepsilon', \Omega)$ is given by [67]

$$I(\varepsilon, \varepsilon', \Omega) = \frac{1}{\beta^2}\sum_{\omega_n\omega_n'} \frac{1}{i\omega_n - \varepsilon}\frac{1}{i\omega_n' - \varepsilon'}\frac{-2\Omega}{(\omega_n - \omega_n')^2 - \Omega^2}. \quad (6)$$

Finally, the electron-phonon coupling constant $g_{\nu\boldsymbol{q},ij}$ and the screened Coulomb interaction $V_{ab,ij}(\omega)$ are calculated by the Kohn-Sham orbital as follows:

$$[g_{\nu\boldsymbol{q},ij}]_{\lambda\lambda'} = \sum_\sigma \int d\boldsymbol{r}[\vec{\varphi}_i]_{\sigma\lambda}(\boldsymbol{r})V_{\nu\boldsymbol{q}}^{\mathrm{BO}}(\boldsymbol{r})[\vec{\varphi}_j^\dagger]_{\lambda'\sigma}, \quad (7)$$

$$V_{ab,ij}(\omega) = \int d\boldsymbol{r}d\boldsymbol{r}' V_{\mathrm{scr}}(\boldsymbol{r}, \boldsymbol{r}', \omega) \times \mathrm{Tr}\left[\left[\vec{\varphi}_i(\boldsymbol{r})\vec{\varphi}_j^\dagger(\boldsymbol{r})\right]\sigma_b^T\left[\vec{\varphi}_j(\boldsymbol{r}')\vec{\varphi}_i^\dagger(\boldsymbol{r}')\right]\sigma_a^T\right], \quad (8)$$

where $V_{\nu\boldsymbol{q}}^{\mathrm{BO}}(\boldsymbol{r})$ is the gradient of the electronic Kohn-Sham potential with respect to the nuclear coordinates [67] and $V_{\mathrm{scr}}(\boldsymbol{r}, \boldsymbol{r}', \omega)$ is the screened Coulomb potential evaluated by the random phase approximation (RPA) or the static Thomas-Fermi approximation [70,71]. Solving Eq. (2) with Eqs. (3)–(8) numerically, we obtain both the even-parity ($a = 0$) and

the odd-parity ($a = x, y, z$) gap function Δ_i^a with the corresponding critical temperature T_c. The superconducting order parameter $\chi_a(\boldsymbol{r}, \boldsymbol{r}')$ is obtained through Eq. (1). Here we evaluate the transition temperature of odd-parity superconductivity by assuming that only one component of the $\boldsymbol{d}$ vector is finite, while this treatment is exact only in the case without the spin-orbit coupling.

The actual calculations are carried out as follows: We calculate the normal-state Kohn-Sham orbital by Quantum ESPRESSO [72,73], which employs the plane wave basis and the pseudopotential to describe the Kohn-Sham orbital and the crystalline potential, respectively. The phonon frequencies and electron-phonon coupling vertices are calculated by using density functional perturbation theory [74]. In the SCDFT calculation we use and extend our open-source program package SUPERCONDUCTING TOOLKIT [75]. We use the GGA-PBE exchange correlation functional [76] and norm-conserved pseudopotentials in the calculations, and check the convergence by increasing energy cutoff for the Kohn-Sham orbital. 12^3 (10^3) regular $\boldsymbol{k}$-point grid for the electronic structure calculations, 6^3 (5^3) $\boldsymbol{q}$-point grid for the phonon calculations, and 40^3 (30^3) $\boldsymbol{k}$-point grid for calculating the density of states are employed in the case of $Sn_{1-x}In_xTe$ ($Cu_xBi_2Se_3$) [71]. The structure optimization is performed for SnTe and InTe, and the lattice constants $a_{SnTe} = 6.39$ Å and $a_{InTe} = 6.25$ Å are obtained, which are slightly larger than those in experiments. The doping dependence is simulated with the carrier doping by using the jellium background insertion [77,78] with the interpolated lattice constants [79]. For $Cu_xBi_2Se_3$ we use the experimental lattice constants due to the difficulty of estimating the c-axis lattice parameter of the van der Waals layered material.

B. Experiment

Single crystals of $Sn_{1-x}In_xTe$ were grown by chemical vapor transport. First stoichiometric amounts of high-purity elements with an In concentration of 10% were sealed into evacuated quartz glass tubes and kept at 950 °C for 48 h. Then the quartz tube was kept at 630 °C for one week which turned out to be sufficient to produce chemically transported shiny facetlike samples. Their sizes varied from a few 100 μm^3 to ∼1 mm^3. The superconducting T_c of various pieces was estimated by measuring the respective jumplike transition in heat capacity in a commercially available system [physical property measurement system (PPMS) equipped with a 3He refrigerator, Quantum Design]. A piece with a mass of about 3.5 mg and $T_c = 1.8$ K was picked up for tunneling spectroscopy measurements. Its In concentration $x = 0.09 \pm 0.01$ was measured with a scanning-electron microscope equipped with an energy-dispersive x-ray (SEM- EDX; JEOL and Bruker) analyzer. We note that x and T_c agree with the published phase diagram in Ref. [51].

Tunneling spectroscopy measurements of $Sn_{0.91}In_{0.09}Te$ were conducted using a dilution refrigerator scanning tunneling microscope (STM) [80] at $T \sim 90$ mK. Because $Sn_{0.91}In_{0.09}Te$ samples used in this study were too small to prepare clean and flat surfaces for scanning and we are interested in the tunneling spectrum only, we glued the samples on the STM tip and formed the junction against a clean Au(100) surface. The samples were cleaned by filing in ultrahigh vacuum.

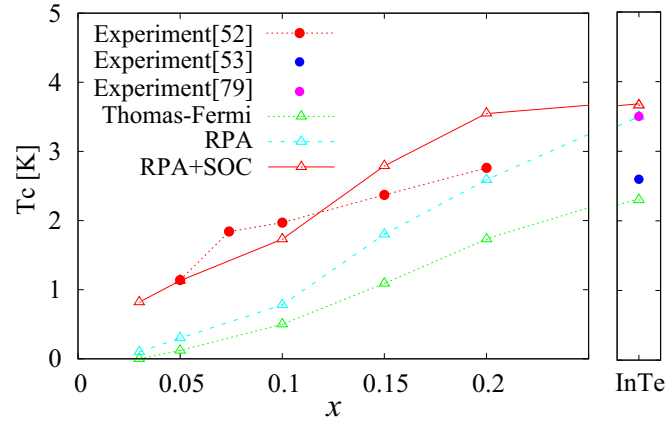

FIG. 1. Transition temperature T_c of $Sn_{1-x}In_xTe$ as a function of x. Filled circles indicate experimental data (red, blue, and magenta data are taken from Refs. [52,53,81,82], respectively). Open triangles show our SCDFT results: red, cyan, and green correspond to those using RPA with the spin-orbit coupling, RPA, and the Thomas-Fermi approximation without the spin-orbit coupling, respectively.

III. RESULTS AND DISCUSSION

In this section we show the results obtained by our SCDFT calculation considering the spin-orbit coupling and odd-parity pairing. We discuss basic properties of $Sn_{1-x}In_xTe$ including transition temperatures, momentum dependence of the gap functions, and local density of states (DOS) in the superconducting states. We perform a tunneling spectroscopy measurement and compare it with the calculation. Our results show that the odd-parity states are never realized as the leading states in $Sn_{1-x}In_xTe$. We discuss whether the conventional even-parity superconductivity explains the experimental observations and why the odd-parity superconductivity is not realized in the present formalism of SCDFT.

First of all, in Fig. 1 we show the transition temperatures T_c calculated with the several approximations for $Sn_{1-x}In_xTe$. Filled circles indicate experimental data, and open triangles are our SCDFT results. As a usual BCS superconductor, we find that T_c obtained by RPA is higher than that by the Thomas-Fermi approximation at any x. This is because any pairing channel through the charge dynamics, such as the plasmon channel known to enhance T_c, is not included in the Thomas-Fermi approximation. In the low doped region, however, we find that the RPA results without the spin-orbit coupling still underestimate T_c compared to the experiments. The doping dependence of T_c is almost the same as the previous calculation obtained by the McMillan formula, which implies that the charge fluctuation is not the only reason for the discrepancy between the theory and the experiment [53].

Our finding is that the spin-orbit coupling dramatically improves the situation as shown by the red triangles in Fig. 1. We can see that obtained T_c is strongly enhanced and reaches about 4 times as large as that without the spin-orbit coupling at $x = 0.05$, which is well-consistent with the experimental value. It is worth noting that the enhancement of T_c by the

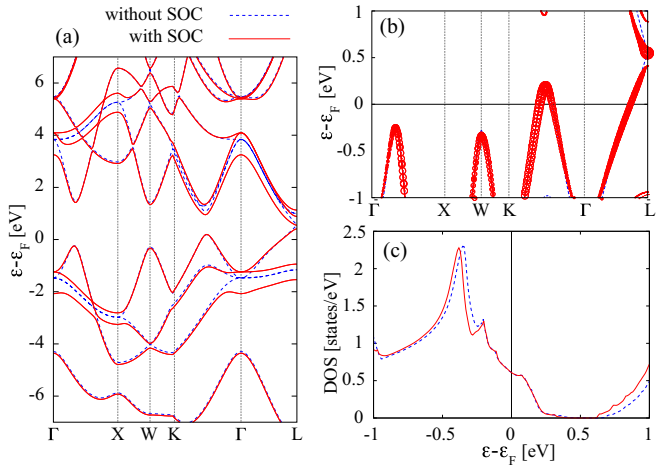

FIG. 2. (a) Band structures of $Sn_{0.9}In_{0.1}Te$ and (b) enlarged one near the Fermi level with (solid red lines) and without (dashed blue lines) the spin-orbit coupling. The size of red circles in (b) indicates the weight of Sn-*s* orbital. (c) The density of states of $Sn_{0.9}In_{0.1}Te$ near the Fermi level.

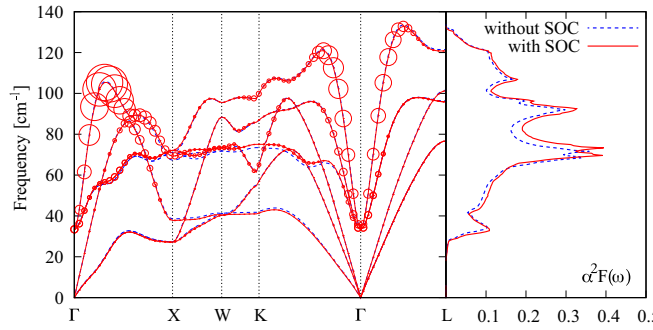

FIG. 3. Left panel: Phonon dispersion relations of $Sn_{0.9}In_{0.1}Te$ with (solid red lines) and without (dashed blue lines) the spin-orbit coupling. Phonon linewidth $\gamma_{q\nu}$ for the case with the spin-orbit coupling is indicated by the size of the circle. Right panel: Calculated Eliashberg function $\alpha^2F(\omega)$ both with and without the spin-orbit coupling. Electron-phonon coupling constant λ is $\lambda \approx 0.36$ (0.30) when the spin-orbit coupling is considered (neglected).

spin-orbit coupling appears to become stronger at the lower doped region. For InTe, we cannot find such large deviation between relativistic and nonrelativistic calculation. As shown in the right panel of Fig. 1, both results agree with the experimental T_c, which indicates less importance of the spin-orbit coupling in the limit of $x = 1$. This behavior is counterintuitive in that Sn and In sit next to each other in the periodic table and have a similar size of atomic spin-orbit coupling. It should be noted that such behavior was also found in the elemental superconductors Tl and Pb [83,84], for which there is no simple explanation.

To clarify the origin of this behavior, in the following we present several normal state properties, such as band dispersions, phonon dispersions, and the Eliashberg functions of $Sn_{0.9}In_{0.1}Te$, and compare the results with and without the spin-orbit coupling. Figures 2(a) and 2(b) depict the band structures and Fig. 2(c) DOS near the Fermi level. As is shown in Fig. 3, the Debye frequency of $Sn_{0.9}In_{0.1}Te$ is around $120\,\mathrm{cm}^{-1} \sim 15$ meV, which is comparably small to elemental Pb. We find that both the band and DOS structures is not changed by including the spin-orbit coupling within the energy window of 200 meV near the Fermi level. Thus, we can conclude that the large enhancement of T_c by the spin-orbit coupling does not come from the purely electric origin but from the changes in the phonon property such as the coupling strength with the electrons. While it is known that the spin-orbit coupling also affects the screened Coulomb interaction in strongly correlated electron systems [85,86], we confirmed that its effect is not significant to the enhancement of T_c in $Sn_{1-x}In_xTe$ [87].

Figure 3 shows the phonon dispersion relations $\Omega_{q\nu}$ with the linewidth $\gamma_{q\nu}$ and the Eliashberg function $\alpha^2F(\omega)$ (the effective pairing interaction due to electron-phonon coupling),

$$\alpha^2F(\omega) = \frac{1}{2\pi D}\sum_{q\nu}\delta(\omega - \Omega_{q\nu})\frac{\gamma_{q\nu}}{\hbar\Omega_{q\nu}}, \tag{9}$$

where D is DOS at the Fermi level. The overall structure of the phonon dispersion is consistent with the previous calculations [88,89] and the neutron experiment [90]. We find that, although the phonon dispersion is slightly pushed up near $\Omega_{q\nu} \sim 60\ \mathrm{cm}^{-1}$, it is almost unchanged by including the spin-orbit coupling. However, compared to the electronic and phonon dispersions, $\alpha^2F(\omega)$ is more sensitive. We can see that $\alpha^2F(\omega)$ with the spin-orbit coupling is larger than that without the spin-orbit coupling over almost all range of ω. As a result, the electron-phonon coupling constant defined by $\lambda = 2\int_0^\infty d\omega\alpha^2F(\omega)/\omega$ becomes $\lambda \approx 0.36$, which is larger than that without the spin-orbit coupling by 20%. According to the McMillan formula, the transition temperature at a weak coupling region is highly sensitive to the small change of λ, and that is why very strong enhancement of T_c by the spin-orbit coupling is observed at a lower doped region. Note that such enhancement of λ is known for elemental Pb [83,84] where λ increases 50% when the spin-orbit coupling is included. However, there is no such enhancement of T_c because Pb is in the strong coupling regime, and thus the change of λ has less effect on T_c than $Sn_{1-x}In_xTe$. We also calculate λ based on the electronic and phonon structures of SnTe simply by changing the chemical potential. The results are shown in Fig. 4(a). Figure 4(a) clearly shows that the spin-orbit coupling has more significant effect on the electron-phonon coupling at a low doped region. This can be seen more clearly by λ/D in Fig. 4(b), which is proportional to g^2 and purely reflects the change of the electron-phonon coupling strength. Although various effects are highly coupled and difficult to disentangle, this may be explained by the orbital mixing effect due to the band inversion at L points, which is the relevant feature of SnTe as the topological crystalline insulator [35].

Another notable feature is the presence of soft optical phonon modes at Γ point as shown in Fig. 3. Actually, the coupling between electrons and such phonon modes has been proposed as the candidate mechanism of odd-parity superconductivity of $Sn_{1-x}In_xTe$ [54]. In our calculations, the $\boldsymbol{q}$ dependent coupling constant $\lambda_{\boldsymbol{q}}$, and also $\gamma_{q\nu}$, are enhanced around Γ point due to the presence of the soft phonon modes, which usually favors the odd-parity pairing states than

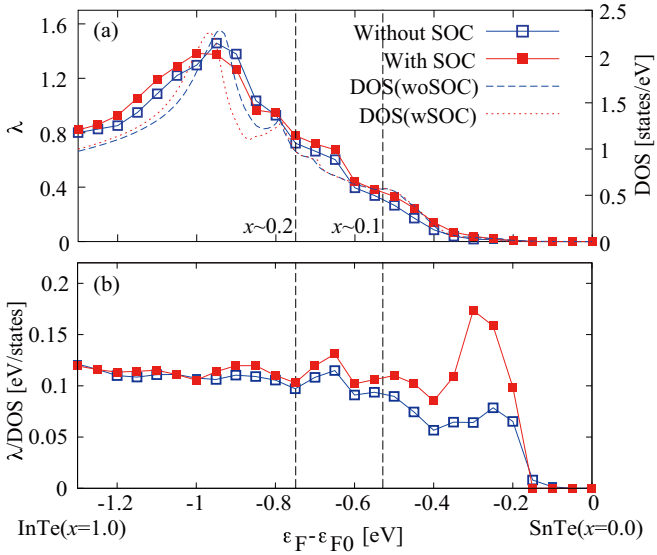

FIG. 4. (a) Electron-phonon coupling constant λ as a function of the chemical potential (solid line). Dashed lines show the density of states. (b) λ divided by the density of states. Red and blue lines are the results with and without the spin-orbit coupling, respectively.

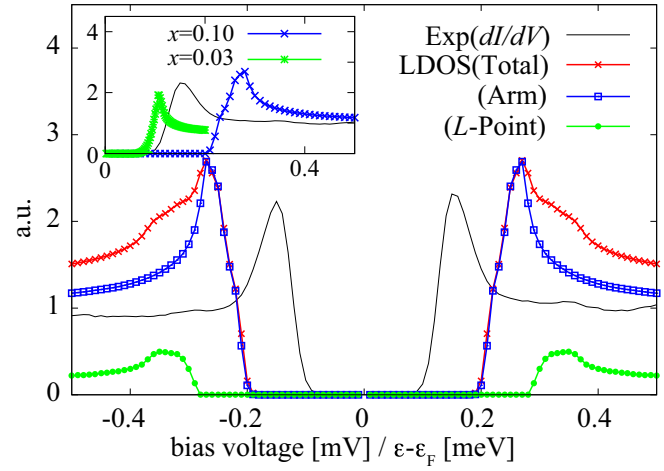

FIG. 6. Local DOS in the superconducting phase of $Sn_{0.9}In_{0.1}Te$ (red) and dI/dV curve of the sample with $T_c = 1.8$ K (black). Green and blue lines correspond to separate contributions from the Fermi surface around L points and from armlike regions bridging L points, respectively. Note that the dI/dV curve in the experiment shows almost symmetric behavior below and above the Fermi energy. Inset shows contribution from the armlike region for $x = 0.03$ (green), 0.1 (blue), and dI/dV curve (black).

the even-parity ones. However, our calculations show that the anomalous $\boldsymbol{q}$ dependence we observed is not significant enough so that the odd-parity paring instability exceeds the conventional s-wave paring with small anisotropy.

Finally, we show the obtained momentum dependence of even-parity and odd-parity gap functions in Fig. 5. Since it is difficult to evaluate the actual transition temperature of odd-parity pairing states due to its too weak instability, we show the results obtained by solving linearized gap equation (2). In Fig. 5 we can see that the leading s-wave gap function is anisotropic in that the maximum value is about twice as large as the minimum value, which cannot be obtained in the absence of the spin-orbit coupling. On the other hand, the odd-parity gap function has a clear p-wavelike momentum dependence, although the eigenvalue λ_g of the linearized gap equation is around 0.1 at the transition temperature of the leading s-wave superconductivity. It should be noted that we

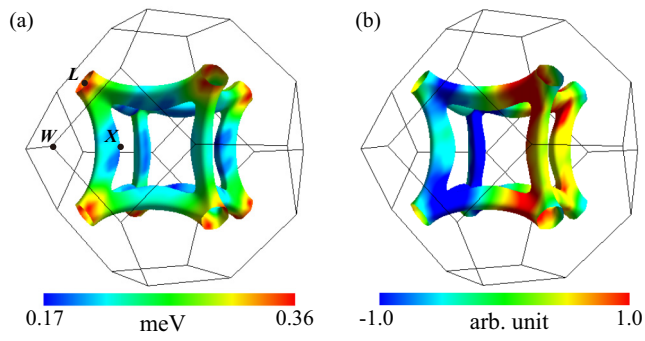

FIG. 5. Fermi surface of $Sn_{0.9}In_{0.1}Te$ colored by the superconducting gap amplitude with (a) leading s-wave and (b) p-wave gap. The p-wave gap function is obtained by the linearized gap equation and thus the amplitude should be regarded as the arbitrary unit. They are drawn by using FermiSurfer [91].

calculated the temperature dependence of λ_g for the odd-parity pairing varying In concentration x without assuming gap representations, and found that the maximum ratio of T_c for p-wave and s-wave pairing never exceeds 0.1. Thus, we conclude that, at least within our SCDFT calculations, the even-parity s-wave is the most stable gap symmetry in $Sn_{1-x}In_xTe$.

In the following we compare the results based on SCDFT and tunneling spectroscopy measurement. Since the transition temperature of the sample is about 1.8 K, we show the data of $Sn_{0.9}In_{0.1}Te$ as the reference calculation. Figure 6 shows local DOS in the superconducting phase obtained by SCDFT and corresponding dI/dV curve in the tunneling spectroscopy measurement. As mentioned above, the gap function in the presence of the spin-orbit coupling has clear anisotropy in the momentum space that the gap amplitude around the L points is about twice larger than that on the armlike regions connecting them. That gives rise to a shoulderlike structure above 0.30 meV in addition to the conventional BCS-type anomaly around 0.25 meV, which does not exist in the experimental observation in the dI/dV curve. This discrepancy may be understood by considering the momentum dependence of the tunneling probability in the tunneling spectroscopy measurement: if the tunneling spectrum is more sensitive to the gap function on the armlike regions than that around the L points, the single BCS-type anomaly corresponding to the small gap amplitude is observed. Indeed, the orbital character of $Sn_{1-x}In_xTe$ strongly depends on the crystal momentum. As is shown in Fig. 2(b), the contribution of the Sn-s orbital around the L points is suppressed due to the band inversion. Since the s orbital is spatially spread and isotropic, we can expect that the tunneling probability of the armlike region is higher than that of the L points. Actually, the separate contribution from the armlike regions to the local

DOS (blue line in Fig. 6) agrees better with the dI/dV curve. Although the experimental gap amplitude is slightly smaller than the calculation, the value falls between the calculations at $x = 0.03$ and $x = 0.1$ (inset of Fig. 6). These results as well as the carrier-density dependence of T_c (Fig. 1) suggest that the conventional s-wave superconductivity is realized in $Sn_{1-x}In_xTe$.

IV. CONCLUSION

In this paper we combined the first-principles SCDFT calculations and tunneling spectroscopy measurements to unveil the microscopic gap functions and mechanism of superconductivity in $Sn_{1-x}In_xTe$. We extend SCDFT to deal with the spin-orbit coupling and the odd-parity superconductivity. Our SCDFT successfully reproduces the critical temperature of $Sn_{1-x}In_xTe$ quantitatively and reveals that the spin-orbit coupling largely enhances it in the low carrier region. We find that the enhancement of T_c mainly comes from that of the electron-phonon coupling constant, as is observed in the elemental Pb but not in Tl [83,84], although the intuitive mechanism of it remains an open issue. The leading gap function is a conventional s wave with some anisotropy, which is consistent with the obtained spectrum in the tunneling spectroscopy measurements. Our theory and experiment indicate that the superconductivity in $Sn_{1-x}In_xTe$ can be understood by the conventional s-wave scenario without introducing topologically nontrivial spin-triplet superconductivity.

ACKNOWLEDGMENTS

This work was supported by a Grant-in-Aid for Scientific Research (No. 15K05140, No. 16H06345, No. 17H02770, No. 18K03442, and No. 19K14654) from Ministry of Education, Culture, Sports, Science and Technology. T.N. is supported by RIKEN Special Postdoctoral Researchers Program. M.Ka. was supported by Priority Issue (creation of new functional devices and high-performance materials to support next generation industries) to be tackled by using Post 'K' Computer from the MEXT of Japan.

APPENDIX: SCDFT RESULTS FOR $Cu_xBi_2Se_3$

Here we summarize SCDFT results for $Cu_xBi_2Se_3$ to compare with the $Sn_{1-x}In_xTe$ superconductor. In contrast to $Sn_{1-x}In_xTe$, we cannot obtain a converged solution belonging to the odd-parity representation even for the linearized gap equation. This result suggests that odd parity pairing states are far less likely to be realized by the conventional phonon-mediated mechanism in this compound. The main origin can be seen from the momentum dependence of the phonon linewidth $\gamma_{\boldsymbol{q}\nu}$ shown in Fig. 7(a). Although it has some anisotropy, any anomalous enhancement near the acoustic phonon branches, which is the driving force to induce the spin-triplet superconductivity discussed in Ref. [59], is not observed in our calculations. Thus, the $\boldsymbol{q}$ dependence of the repulsive interaction reflecting the nature of bare Coulomb interaction overcomes that of the attractive interaction arising from the electron-phonon coupling, which generally disfavors the odd-parity pairing states. On the other hand, a color map

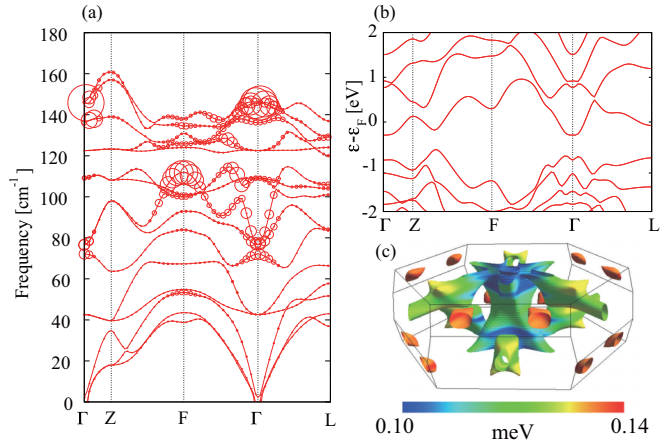

FIG. 7. (a) Phonon dispersion relations of $Cu_{0.2}Bi_2Se_3$ with the phonon linewidth $\gamma_{\boldsymbol{q}\nu}$ indicated as the size of the circles (the spin-orbit coupling is included). (b) Band structure near the Fermi surface. (c) Fermi surface colored by the superconducting gap amplitude of the s-wave solution. This is drawn by using FermiSurfer [91].

of the gap amplitude on the Fermi surface in Fig. 7(c) shows slight momentum dependence along k_z axis even in the s-wave superconductivity. Our results and the fact that the triplet gap function discussed in Ref. [59] has a sign change along the k_z axis may indicate that the k_z dependent gap function is a general feature of electron doped Bi_2Se_3.

Figure 8 shows calculated transition temperatures of $Cu_xBi_2Se_3$ and the experimental values from Ref. [32]. In contrast to $Sn_{1-x}In_xTe$, we see that the transition temperatures of $Cu_xBi_2Se_3$ cannot be reproduced even qualitatively by using the even-parity pairing solutions. Because DOS near the Fermi level strongly affects the transition temperature and monotonically increases as a function of x at the low carrier region in the calculations, the nonmonotonic behavior of the electron density in experiments [33] may cause the discrepancy between the calculations and experiments. Another possibility is that the superconductivity of $Cu_xBi_2Se_3$ is not

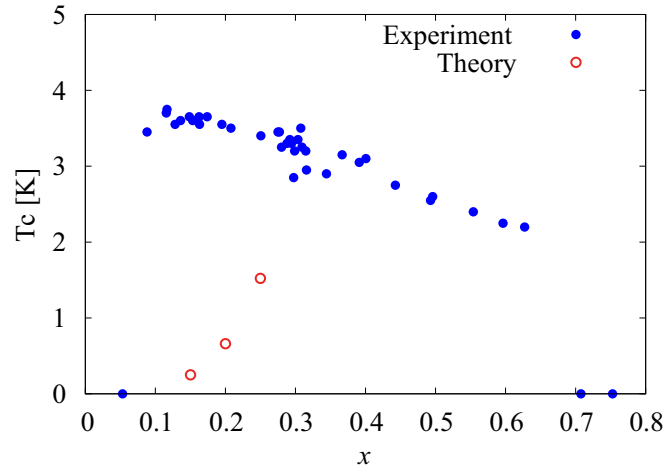

FIG. 8. Transition temperatures of $Cu_xBi_2Se_3$ obtained by SCDFT (open red circles) and the experiment values (filled blue circles) [32].

mediated by phonon but by other unconventional mechanisms such as magnetic fluctuations. Indeed, there are many examples of the low-carrier density superconductors including Li_xHfNCl [92] and $LaO_{1-x}F_xBiS_2$ [93], whose transition temperatures are considerably underestimated by SCDFT. Some of these superconductors are stabilized by a nonphonon type pairing mechanism. Our results may indicate that $Cu_xBi_2Se_3$ belongs to the same category of unconventional superconductivity as these materials. Considering other fluctuation-mediated mechanisms in the framework of SCDFT is an interesting topic [94] to study but beyond the scope of this paper. We leave it as a future study.

[1] N. Read and D. Green, Phys. Rev. B **61**, 10267 (2000).
[2] X.-L. Qi, T. L. Hughes, S. Raghu, and S.-C. Zhang, Phys. Rev. Lett. **102**, 187001 (2009).
[3] X.-L. Qi and S.-C. Zhang, Rev. Mod. Phys. **83**, 1057 (2011).
[4] Y. Ando and L. Fu, Annu. Rev. Condens. Matter Phys. **6**, 361 (2015)
[5] M. Sato and Y. Ando, Rep. Prog. Phys. **80**, 076501 (2017).
[6] C. Nayak, S. H. Simon, A. Stern, M. Freedman, S. Das Sarma, Rev. Mod. Phys. **80**, 1083 (2008).
[7] J. Alicea, Rep. Prog. Phys. **75**, 076501 (2012).
[8] C. W. J. Beenakker, Annu. Rev. Condens. Matter Phys. **4**, 113 (2013).
[9] M. Sato and S. Fujimoto, J. Phys. Soc. Jpn. **85**, 072001 (2016).
[10] M. Sato, Phys. Lett. B **575**, 126 (2003).
[11] L. Fu and C. L. Kane, Phys. Rev. Lett. **100**, 096407 (2008).
[12] M. Sato, Y. Takahashi, and S. Fujimoto, Phys. Rev. Lett. **103**, 020401 (2009).
[13] R. M. Lutchyn, J. D. Sau, and S. Das Sarma, Phys. Rev. Lett. **105**, 077001 (2010).
[14] Y. Oreg, G. Refael, and F. von Oppen, Phys. Rev. Lett. **105**, 177002 (2010).
[15] V. Mourik, K. Zuo, S. M. Frolov, S. R. Plissard, E. P. A. M. Bakkers, L. P. Kouwenhoven, Science **336**, 1003 (2012).
[16] M. T. Deng, C. L. Yu, G. Y. Huang, M. Larsson, P. Caroff, and H. Q. Xu, Nano Lett. **12**, 6414 (2012).
[17] A. D. K. Finck, D. J. Van Harlingen, P. K. Mohseni, K. Jung, and X. Li, Phys. Rev. Lett. **110**, 126406 (2013).
[18] S. Nadj-Perge, I. K. Drozdov, J. Li, H. Chen, S. Jeon, J. Seo, A. H. MacDonald, B. A. Bernevig, and A. Yazdani, Science **346**, 602 (2014).
[19] G. Koren and T. Kirzhner, Phys. Rev. B **86**, 144508 (2012).
[20] M.-X. Wang, C. Liu, J.-P. Xu, F. Yang, L. Miao, M.-Y. Yao, C. L. Gao, C. Shen, X. Ma, X. Chen, Z.-A. Xu, Y. Liu, S.-C. Zhang, D. Qian, J.-F. Jia, and Q.-K. Xue, Science **336**, 52 (2012).
[21] J.-P. Xu, C. Liu, M.-X. Wang, J. Ge, Z.-L. Liu, X. Yang, Y. Chen, Y. Liu, Z.-A. Xu, C.-L. Gao, D. Qian, F.-C. Zhang, and J.-F. Jia, Phys. Rev. Lett. **112**, 217001 (2014).
[22] J.-P. Xu, M.-X. Wang, Z. L. Liu, J.-F. Ge, X. Yang, C. Liu, Z. A. Xu, D. Guan, C. L. Gao, D. Qian, Y. Liu, Q.-H. Wang, F.-C. Zhang, Q.-K. Xue, and J.-F. Jia, Phys. Rev. Lett. **114**, 017001 (2015).
[23] H.-H. Sun, K.-W. Zhang, L.-H. Hu, C. Li, G.-Y. Wang, H.-Y. Ma, Z.-A. Xu, C.-L. Gao, D.-D. Guan, Y.-Y. Li, C. Liu, D. Qian, Y. Zhou, L. Fu, S.-C. Li, F.-C. Zhang, and J.-F. Jia, Phys. Rev. Lett. **116**, 257003 (2016).
[24] Z.-J. Wang, P. Zhang, G. Xu, L. K. Zeng, H. Miao, X. Xu, T. Qian, H. Weng, P. Richard, A. V. Fedorov, H. Ding, X. Dai, and Z. Fang, Phys. Rev. B **92**, 115119 (2015).
[25] P. Zhang, K. Yaji, T. Hashimoto, Y. Ota, T. Kondo, K. Okazaki, Z. Wang, J. Wen, G. D. Gu, H. Ding, and S. Shin, Science **360**, 182 (2018).
[26] D. Wang, L. Kong, P. Fan, H. Chen, S. Zhu, W. Liu, L. Cao, Y. Sun, S. Du, J. Schneeloch, R. Zhong, G. Gu, L. Fu, H. Ding, and H.-J. Gao, Science **362**, 333 (2018).
[27] A. P. Mackenzie and Y. Maeno, Rev. Mod. Phys. **75**, 657 (2003).
[28] Y. Maeno, S. Kittaka, T. Nomura, S. Yonezawa, and K. Ishida, J. Phys. Soc. Jpn. **81**, 011009 (2012).
[29] Y. S. Hor, A. J. Williams, J. G. Checkelsky, P. Roushan, J. Seo, Q. Xu, H. W. Zandbergen, A. Yazdani, N. P. Ong, and R. J. Cava, Phys. Rev. Lett. **104**, 057001 (2010).
[30] L. A. Wray, S.-Y. Xu, Y. Xia, Y. S. Hor, D. Qian, A. V. Fedorov, H. Lin, A. Bansil, R. J. Cava, and M. Z. Hasan, Nat. Phys. **6**, 855 (2010).
[31] M. Kriener, K. Segawa, Z. Ren, S. Sasaki, and Y. Ando, Phys. Rev. Lett. **106**, 127004 (2011).
[32] M. Kriener, K. Segawa, Z. Ren, S. Sasaki, S. Wada, S. Kuwabata, and Y. Ando, Phys. Rev. B **84**, 054513 (2011).
[33] M. Kriener, K. Segawa, S. Sasaki, and Y. Ando, Phys. Rev. B **86**, 180505(R) (2012).
[34] L. Hao and T. K. Lee, Phys. Rev. B **83**, 134516 (2011).
[35] T. H. Hsieh and L. Fu, Phys. Rev. Lett. **108**, 107005 (2012).
[36] Y. Tanaka, M. Sato, and N. Nagaosa, J. Phys. Soc. Jpn. **81**, 011013 (2012).
[37] A. Yamakage, K. Yada, M. Sato, and Y. Tanaka, Phys. Rev. B **85**, 180509(R) (2012).
[38] S. Sasaki, M. Kriener, K. Segawa, K. Yada, Y. Tanaka, M. Sato, and Y. Ando, Phys. Rev. Lett. **107**, 217001 (2011).
[39] T. Kirzhner, E. Lahoud, K. B. Chaska, Z. Salman, and A. Kanigel, Phys. Rev. B **86**, 064517 (2012).
[40] K. Matano, M. Kriener, K. Segawa, Y. Ando, and G.-q. Zheng, Nat. Phys. **12**, 852 (2016).
[41] S. Yonezawa, K. Tajiri, S. Nakata, Y. Nagai, Z. Wang, K. Segawa, Y. Ando, and Y. Maeno, Nat. Phys. **13**, 123 (2017).
[42] L. Fu and E. Berg, Phys. Rev. Lett. **105**, 097001 (2010).
[43] K. Michaeli and L. Fu, Phys. Rev. Lett. **109**, 187003 (2012).
[44] S.-K. Yip, Phys. Rev. B **87**, 104505 (2013).
[45] L. Fu, Phys. Rev. B **90**, 100509(R) (2014).
[46] Y. Tanaka, Z. Ren, T. Sato, K. Nakayama, S. Souma, T. Takahashi, K. Segawa, and Y. Ando, Nat. Phys. **8**, 800 (2012).
[47] T. Sato, Y. Tanaka, K. Nakayama, S. Souma, T. Takahashi, S. Sasaki, Z. Ren, A. A. Taskin, K. Segawa, and Y. Ando, Phys. Rev. Lett. **110**, 206804 (2013).
[48] A. S. Erickson, J. H. Chu, M. F. Toney, T. H. Geballe, and I. R. Fisher, Phys. Rev. B **79**, 024520 (2009).
[49] G. Balakrishnan, L. Bawden, S. Cavendish, and M. R. Lees, Phys. Rev. B **87**, 140507(R) (2013).

[50] R. D. Zhong, J. A. Schneeloch, X. Y. Shi, Z. J. Xu, C. Zhang, J. M. Tranquada, Q. Li, and G. D. Gu, Phys. Rev. B **88**, 020505(R) (2013).

[51] M. Novak, S. Sasaki, M. Kriener, K. Segawa, and Y. Ando, Phys. Rev. B **88**, 140502(R) (2013).

[52] N. Haldolaarachchige, Q. Gibson, W. Xie, M. B. Nielsen, S. Kushwaha, and R. J. Cava, Phys. Rev. B **93**, 024520 (2016).

[53] M. Kriener, M. Kamitani, T. Koretsune, R. Arita, Y. Taguchi, and Y. Tokura, Phys. Rev. Mater. **2**, 044802 (2018).

[54] S. Sasaki, Z. Ren, A. A. Taskin, K. Segawa, L. Fu, and Y. Ando, Phys. Rev. Lett. **109**, 217004 (2012).

[55] A. P. Schnyder, S. Ryu, A. Furusaki, and A. W. W. Ludwig, Phys. Rev. B **78**, 195125 (2008).

[56] A. Kitaev, in *Advances in Theoretical Physics: Landau Memorial Conference*, edited by V. Lebedev and M. Feigel'man, AIP Conf. Proc. No. 1134 (AIP, New York, 2009).

[57] M. Sato, Phys. Rev. B **79**, 214526 (2009).

[58] M. Sato, Phys. Rev. B **81**, 220504(R) (2010).

[59] X. Wan and S. Y. Savrasov, Nat. Commun. **5**, 4144 (2014).

[60] S. Sugai, K. Murase, S. Katayama, S. Takaoka, S. Nishi, and H. Kawamura, Solid State Commun. **24**, 407 (1977).

[61] P. M. R. Brydon, S. Das Sarma, H.-Y. Hui, and J. D. Sau, Phys. Rev. B **90**, 184512 (2014).

[62] N. Levy, T. Zhang, J. Ha, F. Sharifi, A. A. Talin, Y. Kuk, and J. A. Stroscio, Phys. Rev. Lett. **110**, 117001 (2013).

[63] H. Peng, D. De, B. Lv, F. Wei, and C.-W. Chu, Phys. Rev. B **88**, 024515 (2013).

[64] S. Maeda, R. Hirose, K. Matano, M. Novak, Y. Ando, and G.-q. Zheng, Phys. Rev. B **96**, 104502 (2017).

[65] M. Saghir, J. A. T. Barker, G. Balakrishnan, A. D. Hillier, and M. R. Lees, Phys. Rev. B **90**, 064508 (2014).

[66] J. A. Schneeloch, R. D. Zhong, Z. J. Xu, G. D. Gu, and J. M. Tranquada, Phys. Rev. B **91**, 144506 (2015).

[67] M. Lüders, M. A. L. Marques, N. N. Lathiotakis, A. Floris, G. Profeta, L. Fast, A. Continenza, S. Massidda, and E. K. U. Gross, Phys. Rev. B **72**, 024545 (2005).

[68] M. A. L. Marques, M. Lüders, N. N. Lathiotakis, G. Profeta, A. Floris, L. Fast, A. Continenza, E. K. U. Gross, and S. Massidda, Phys. Rev. B **72**, 024546 (2005).

[69] M. Sigrist and K. Ueda, Rev. Mod. Phys. **63**, 239 (1991).

[70] R. Akashi and R. Arita, Phys. Rev. Lett. **111**, 057006 (2013).

[71] M. Kawamura, R. Akashi, and S. Tsuneyuki, Phys. Rev. B **95**, 054506 (2017).

[72] P. Giannozzi *et al.*, J. Phys.: Condens. Matter **21**, 395502 (2009).

[73] P. Giannozzi *et al.*, J. Phys.: Condens. Matter **29**, 465901 (2017).

[74] S. Baroni, S. de Gironcoli, A. Dal Corso, and P. Giannozzi, Rev. Mod. Phys. **73**, 515 (2001).

[75] http://sctk.osdn.jp/.

[76] J. P. Perdew, K. Burke, and M. Ernzerhof, Phys. Rev. Lett. **78**, 1396 (1997).

[77] This is implemented in Quantum ESPRESSO code [72, 73] and details are found in the document https://www.quantum-espresso.org/Doc/INPUT_PW.html.

[78] In Ref. [52] the resonant impurity state coming from the In-5*s* orbital is discussed for the low doping region of $Sn_{1-x}In_xTe$, which is not captured in this treatment. Although it is an important theoretical challenge to reveal how the resonant state affects the superconducting symmetry and the transition temperature with the phonon calculations, here we focus on the intrinsic properties inherent in SnTe.

[79] For the lattice constants we employ $a_{Sn_{1-x}In_xTe} = a_{SnTe} - a'_{expt}x$, where a'_{expt} is estimated in the experiments [53]. Note that the obtained T_c is not sensitive to the interpolation methods.

[80] T. Machida, Y. Kohsaku, and T. Hanaguri, Rev. Sci. Instrum. **89**, 093707 (2018).

[81] M. Kriener, M. Sakano, M. Kamitani, M. S. Bahramy, R. Yukawa, K. Horiba, H. Kumigashira, K. Ishizaka, Y. Tokura, and Y. Taguchi, arXiv:1901.08739.

[82] In the experiments, two cubic phases of InTe are observed, which show the different lattice constants and the transition temperatures [81]. Our RPA results agrees with the T_c of the sample with the larger lattice constant and higher T_c.

[83] R. Heid, K.-P. Bohnen, I. Yu. Sklyadneva, and E. V. Chulkov, Phys. Rev. B **81**, 174527 (2010).

[84] I. Yu. Sklyadneva, R. Heid, P. M. Echenique, K.-B. Bohnen, and E. V. Chulkov, Phys. Rev. B **85**, 155115 (2012).

[85] C. Martins, M. Aichhorn, and S. Biermann, J. Phys.: Condens. Matter **29**, 263001 (2017).

[86] B. Kim, P. Liu, Z. Ergönenc, A. Toschi, S. Khmelevskyi, and C. Franchini, Phys. Rev. B **94**, 241113(R) (2016).

[87] We estimated the reduction of the screened Coulomb interaction by the spin-orbit coupling and confirmed that its effect on T_c is only $\sim$0.04 K (0.16 K) at $x = 0.05$ (0.10), which amounts to $\sim$12% (20%) of the value without the spin-orbit coupling.

[88] G. A. S. Ribeiro, L. Paulatto, R. Bianco, I. Errea, F. Mauri, and M. Calandra, Phys. Rev. B **97**, 014306 (2018).

[89] In contrast to Ref. [88], we do not find a negative branch of the phonon dispersion even in the SnTe limit. This is because our PBE lattice constant $a = 6.39$ Å is slightly smaller than 6.42 Å in Ref. [88], which can remove the structural instability similar to the LDA calculation [88]. This discrepancy may come from the difference of the pseudopotentials.

[90] E. R. Cowley, J. K. Darby, and G. S. Pawley, J. Phys. C **2**, 1916 (1969).

[91] M. Kawamura, Comput. Phys. Commun. **239**, 197 (2019).

[92] R. Akashi, K. Nakamura, R. Arita, and M. Imada, Phys. Rev. B **86**, 054513 (2012).

[93] C. Morice, R. Akashi, T. Koretsune, S. S. Saxena, and R. Arita, Phys. Rev. B **95**, 180505(R) (2017).

[94] F. Essenberger, A. Sanna, A. Linscheid, F. Tandetzky, G. Profeta, P. Cudazzo, and E. K. U. Gross, Phys. Rev. B **90**, 214504 (2014).